Surface reconstructions on $Mn_3O_4(001)$ films

K. Gillmeister, M. Trautmann, M. Huth, R. Shantyr* K. Meinel, A. Chassé, K.-M. Schindler†
H. Neddermeyer, and W. Widdra
Institut für Physik, Martin-Luther-Universität Halle-Wittenberg, von-Danckelmann-Platz 3, D-06120 Halle, Germany

(Received 13 July 2021; revised 5 April 2022; accepted 20 April 2022; published 12 May 2022)

The structural complexity of surfaces of spinel-like oxides together with the existence of competing phases of different or mixed valencies have limited surface structure determinations so far. Only recently, the concept of subsurface cation vacancies (SCVs) could be demonstrated for an Fe_3O_4 single crystal surface. Here, we present the appearance of SCVs for ultrathin and thin films of $Mn_3O_4(001)$ depending on film thickness. The structures of films grown by molecular beam epitaxy have been investigated using scanning tunneling microscopy (STM), low-energy electron diffraction (LEED), and near-edge x-ray absorption fine structure spectroscopy (NEXAFS). For coverage up to 4 (Mn ions)/(Ag atom) of Mn_3O_4 and an annealing temperature of 640 K, a $p(2 \times 1)$ reconstruction has been observed in STM and LEED. Using NEXAFS, the identity of the manganese oxide has been narrowed down to the spinel Mn_3O_4 and its related vacancy compound γ-Mn_2O_3. Thus the $p(2 \times 1)$ reconstruction corresponds to an $Mn_3O_4(001)$ surface with MnO_2 termination. For a lower annealing temperature of 450 K or thicker films [5 and 10 (Mn ions)/(Ag atom)], additional $p(4 \times 2)$ and $c(4 \times 4)$ reconstructions have been observed. These extra reconstructions stem from lateral shifts of top-sublayer ions induced by SCVs.

DOI: 10.1103/PhysRevB.105.195415

I. INTRODUCTION

Building up on the seminal investigation of NiO films on Ni(111) [1], ultrathin manganese oxide films in the single-layer regime have been grown and investigated on the substrates Pt(111) [2–5], Pd(001) [6–9], Rh(001) [10], Rh(111) [11], Au(111) [12], and Ag(001) [13–19]. In the thin film preparation of transition metal oxides, the oxidation states of metal ions depend on oxygen partial pressure, deposition rate and substrate temperature. Starting with preparation conditions for MnO, an increase in oxygen pressure leads to the formation of the next higher manganese (II,III) oxide, Mn_3O_4, with a mix of Mn^{2+} and Mn^{3+} ions. A further increase in oxygen pressure is expected to result in α- and γ-Mn_2O_3 with Mn^{3+} ions only. In addition to the dependence on oxygen pressure, one on deposition rate has also been reported. The formation of MnO is found for an oxygen pressure of 2×10^{-7} mbar and deposition rates of 2.2 and 1 Å/min [13,16,20], as well as for 2×10^{-8} mbar and 2.2 Å/min [17]. However, for an oxygen pressure of 2×10^{-8} mbar and a deposition rate of 0.4 Å/min, Mn_3O_4 is formed [18,21]. The formation of the higher oxide at low oxygen pressure and deposition rate indicates kinetic rather than thermodynamic control over which oxide forms.

Our discussion of the structures observed builds up on the structural relation of MnO, Mn_3O_4, and γ-Mn_2O_3. Their common structural element is an fcc lattice of oxygen ions. Positions and oxidation states of the manganese ions represent the major differences. In the rock-salt structure of MnO, the Mn^{2+} ions are octahedrally coordinated to six oxygen ions [22]. This leads to the characteristic structural feature that there is only one sort of atomic sublayer in the (001) plane with a one-to-one ratio of manganese and oxygen ions.

The spinel structure of Mn_3O_4 (hausmannite) is obtained from the rock-salt structure of MnO by the removal of two out of four octahedral manganese ions and the addition of one tetrahedral manganese ion in an extra sublayer. This leads to substantial changes in lattice parameters ($a = 576.5$ pm, $c = 944.2$ pm) and atomic distances [Figs. 1(a) and 1(b)]. The structure can be represented by a stack of eight sublayers [Fig. 1(d)] and a Jahn-Teller distortion in c direction [23,24]. All its bulk terminated (001) surfaces are polar, which makes a study of its growth and surface reconstructions an interesting topic.

The third manganese oxide, γ-Mn_2O_3, is obtained from Mn_3O_4 by the creation of additional cation vacancies. Investigations in the late 1950s arrived at controversial results with tetrahedral vacancies by Goodenough *et al.* [25] and octahedral vacancies by Sinha *et al.* [26]). A detailed x-ray diffraction study confirmed tetrahedral vacancies for Mn^{3+}/Mn^{2+} ratios below 2.4 and both vacancies for ratios above 2.4 [27]. For the related iron oxides, Fe_3O_4 and γ-Fe_2O_3, octahedral vacancies have been observed [28,29]. Despite the creation of vacancies, differences in structural parameters of Mn_3O_4 and γ-Mn_2O_3 remain small. On the $Fe_3O_4(001)$ surface, the vacancies induce a $c(2 \times 2)$ reconstruction, where surface layer metal ions relax toward tetrahedral interstitial sites [30].

*Now at: ASML The Netherlands B.V., De Run 6501, 5504 DR Veldhoven, The Netherlands.
†Corresponding author: karl-michael.schindler@physik.uni-halle.de

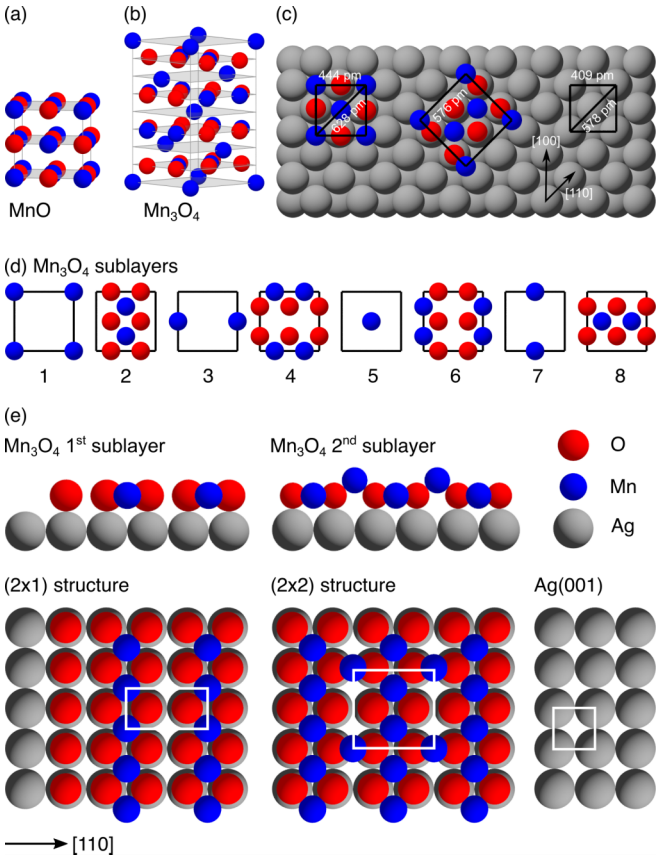

FIG. 1. Hard sphere models of unit cells of (a) rock-salt MnO and (b) spinel Mn_3O_4. (c) Lattice fittings for MnO(001)/Ag(001) (lattice mismatch 8.6%) and 45° rotated Mn_3O_4/Ag(001) (lattice mismatch 0.3%), (d) eight sublayers of the Mn_3O_4 unit cell, and (e) film growth of Mn_3O_4 on Ag(001) for the first and second sublayers. Oxygen, manganese, and silver are represented in red, blue, and grey, respectively.

For Mn_3O_4, the growth of ultrathin films has been examined on $SrTiO_3$(100) and (111) [31–35], MnO(001) [36], Si(100) [37,38], and Au(111) [12]. Regarding Mn_3O_4 on Ag(001), there is only one report focusing on LEED and XPS [39], but no investigations of the microscopic real-space structure have been reported. In agreement with and close reference to a preliminary version of this publication [40], they report an apparent $p(2 \times 2)$ reconstruction, which actually is a superposition of a $c(2 \times 2)$ reconstruction and twofold domains of a $p(2 \times 1)$ reconstruction. In addition, they report a $p(2 \times 5)$ reconstruction for films grown with the substrate at 473 K [39].

The Mn_3O_4 films grow with their in-plane ⟨100⟩ directions parallel to the in-plane ⟨110⟩ directions of the underlying Ag(001) lattice. This rotation of the Mn_3O_4 unit cell by 45° yields a (2×2) LEED pattern with respect to the Ag(001) substrate exactly as found for Mn_3O_4(001) on MnO(001) [36]. Such a 45° rotation has also been observed for other substrates, e.g., LiF, KCl, and NaI on MgO(001) [41] and NaCl on Ag(001) [42]. According to the "roles of lattice fitting in epitaxy" [41], a 45° rotated orientation is expected, if the ratio $a_{\text{film}}/a_{\text{substrate}}$ of the lattice parameters is close to $\sqrt{2}$. For a 45° rotated growth of Mn_3O_4(001) on Ag(001) ($a_{\text{Ag}} = 409$ pm, $a_{Mn_3O_4} = 576$ pm [23]) the mismatch of 0.3% becomes negligible (Fig. 1). Consequently, one can expect a perfect film structure if growing Mn_3O_4(001) films on Ag(001) contrary to MnO(001) films on Ag(001). Figure 1(e) shows the expected arrangement of ions in the first and second sublayers of Mn_3O_4(001) on Ag(001). Please note that we assume the mixed sublayer of Mn and O at the interface simply because this sublayer is closer packed than the Mn sublayer and therefore fits better to the close packed top layer of the Ag substrate.

Ultrathin and thin manganese oxide films have been prepared on a Ag(001) substrate by means of reactive Mn deposition in O_2 atmosphere [43]. From NEXAFS spectra, chemical phase identities and lattice orientations were determined. Film morphologies, island shapes, and reconstructions on island surfaces were studied with STM and LEED, starting from initial islands up to a coverage of 3 nm of Mn_3O_4, which corresponds to 10 Mn ions per Ag atom of the substrate surface. This has enabled us to further elaborate the surface reconstructions and relate them to subsurface cation vacancies known from Fe_3O_4 films [30] and bulk manganese oxides [25,26].

II. EXPERIMENTAL

Experiments have been performed using three ultra-high vacuum (UHV) systems. The first one is equipped with an STM, spot profile analysis (SPA)-LEED optics, and a cylindrical mirror analyzer (CMA) for Auger electron spectroscopy (AES). All presented LEED patterns have been recorded as 2D scans with commercial SPA-LEED optics from Omicron as described previously [44,45]. Please note that the 2D LEED patterns recorded with these optics contain the (0 0) spot. The second system contains conventional LEED optics and a low-temperature STM, operating at 100 K. The base pressures of both chambers were in the low 10^{-10} mbar range. In addition, a third UHV chamber was used for NEXAFS studies at the beamline UE56-2 PGM-2 (energy range: 100-1000 eV) at the synchrotron radiation facility BESSY II [46]. NEXAFS spectra have been recorded in total electron yield mode with linear polarization of the x rays and an energy resolution below 100 meV. They have been normalized to the incident x-ray flux using the photocurrent from the last refocusing mirror of the beamline.

The Ag(001) crystals (miscut $<0.2°$) were cleaned by cycles of Ar+ ion sputtering (600 V, 2μA) at room temperature and subsequent heating at 630 K until they showed a clean, defect-free surface in STM and sharp spots in the LEED pattern. Metallic manganese was evaporated from Ta crucibles heated by electron bombardment. Deposition rates were calibrated by means of a quartz microbalance, AES, and STM and controlled by monitoring the flux of Mn ions as reported previously [4]. Deposition rates will be given in (Mn ions)/(Ag substrate atom × min), because the ion flux is the quantity under direct experimental control, whereas the commonly used film thickness in Å or monolayers depend on the structure of the film. For MnO films a nearly layer-by-layer pseudomorphic growth is obtained with a 1:1 ratio of Mn ions to Ag substrate atoms. Assuming bulk structure and neglecting relaxations at the interface and in the film, one

monolayer corresponds to a film thickness of half of the lattice constant a of the unit cell, i.e., 222 pm [22].

Mn_3O_4 is more difficult, because the structure presents two types of sublayers with different amounts of Mn ions [23]. The MnO_2 sublayer has a 0.5:1 ratio of Mn ions to Ag substrate atoms, the Mn sublayer a ratio of 0.25:1. The combination of these two sublayers results in the formula unit Mn_3O_4 and has a ratio of Mn ions to Ag substrate atoms of 0.75:1. In some context, the concept of a double sublayer is convenient. Assuming bulk structure, such a double sublayer corresponds to a quarter of the lattice constant c of the unit cell, i.e., 236 pm. An odd number of sublayers requires the thickness of either of the two types of sublayers and the thickness depends on the termination. Specifying the number of sublayers avoids these problems and yields a better idea of the geometric structure than a thickness in angstroms or nanometers.

For the same flux of Mn ions a film thickness given in angstroms or nanometers depends strongly on the structure. For example, 3 (Mn ions)/(Ag atom) yield 3 sublayers (0.67 nm) of MnO, but 8 sublayers (0.94 nm) of Mn_3O_4. Therefore we prefer to specify the number of metal ions per (1×1) unit cell of the substrate, in short Mn/Ag. It also avoids the recalculation of the thickness after a revision of the structure. For large amounts, the conversion from number of Mn/Ag to thickness of an Mn_3O_4 film in pm can be approximated by a factor of 314.7.

The deposition was performed at sample temperatures of 450 K or room temperature, 295 K. The local film morphology was characterized by STM in constant current mode, the spatially averaged phase symmetry by LEED. The equivalence of films obtained in different UHV systems was ensured using LEED.

III. RESULTS

A. NEXAFS of MnO and Mn_3O_4

In the following, LEED and NEXAFS are used to identify the films prepared at different oxygen partial pressures. For MnO(001) films on Ag(001), 4 Mn/Ag have been deposited by reactive evaporation in 5×10^{-8} mbar O_2 with the Ag(001) substrate at room temperature. Annealing the film to approximately 800 K results in brilliant and sharp LEED spots showing the (1×1) pattern of MnO(001) as reported previously [13,17,20]. Assuming layer-by-layer growth of MnO, the film has a thickness of four layers. Neglecting the vertical expansion due to the lateral compression, four layers correspond to a film thickness of 0.89 nm.

NEXAFS spectra at the oxygen K absorption edge of the MnO film on Ag(001) are depicted in Fig. 2(a). The spectra agree with published spectra of MnO films grown on Ag(001) [15] and are characteristic for MnO(001) [47]. They show only a minor linear dichroism for normal (0°) and grazing light incidence (70° off-normal). This NEXAFS dichroism indicates small deviations from a cubic bulk-like structure of MnO (Fig. 1). In the bulk, the octahedral coordination of Mn ions to six O ions is an isotropic environment and the spectra do not depend on the angle of light incidence or polarization. At the surface, the reduced coordination of Mn ions in the top sublayer can cause the dichroism as observed in the spectra.

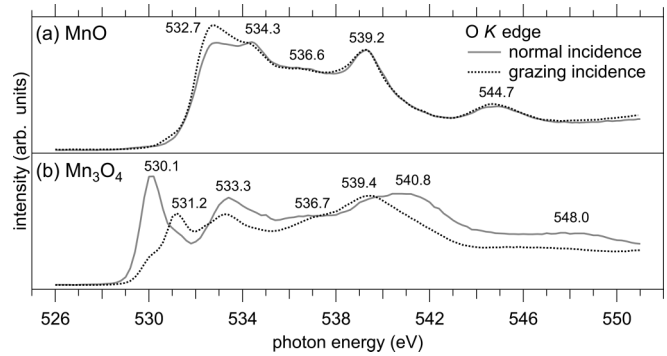

FIG. 2. NEXAFS spectra of (a) MnO, 4 Mn/Ag and (b) Mn_3O_4, 20 Mn/Ag on Ag(001) for normal and grazing x-ray incidence (gray and black dashed, respectively). For details of preparation conditions and the discussion see text section A.

On Ag(001), ultrathin MnO films grow strained because of the lattice mismatch between Ag and MnO. With a thickness of four layers the film is not yet relaxed to the bulk structure, but exhibits a lateral compression and a corresponding vertical expansion [20]. The resulting reduction in symmetry from cubic to tetragonal can also contribute to the small linear dichroism in Fig. 2(a) at 532.7 eV.

The onset of the absorption edge can be assigned to transitions from oxygen 1s core states to 2p states hybridized with manganese 3d orbitals. Therefore the oxidation state of Mn plays an important role [48]. A d^5 configuration (Mn^{2+}) with octahedral symmetry leads to two unoccupied manganese 3d orbitals. The first two peaks at the onset of the absorption edge can thus be assigned to spin-down $t_{2g} \downarrow$ (532.7 eV) and $e_g \downarrow$ (534.3 eV) states. Their splitting of 1.6 eV agrees well with a calculated molecular orbital splitting of 1.4 eV [49].

To obtain the oxygen richer Mn_3O_4 films, the O_2 pressure during Mn evaporation was increased systematically. After growth in an O_2 pressure of 5×10^{-7} mbar, LEED pattern and NEXAFS spectra change. The LEED spots become sharp and brilliant again. Depending on coverage, a $p(2 \times 1)$ or a $p(2 \times 2)$ reconstruction relative to the Ag(001) substrate develops. These reconstructions correspond to a pseudomorphic Mn_3O_4 film rotated by 45° around the surface normal. The rotation by 45° is visualized schematically in Fig. 1(c). Proposed structures of the $p(2 \times 1)$ and $p(2 \times 2)$ reconstructions are presented in Fig. 1(e).

Figure 2(b) shows NEXAFS spectra at the O K edge for an Mn_3O_4(001) film on Ag(001). For this film, 20 Mn/Ag have been deposited. Neglecting the presence of cation vacancies, this yields an average thickness of 6.4 nm and corresponds to 54 sublayers. The NEXAFS spectra show seven resonances at 530.1, 531.2, 533.3, 536.7, 539.4, 540.8, and 548.0 eV. The energies of all resonances agree well with those in electron energy loss fine structure and NEXAFS spectra of bulk Mn_3O_4 [48,50–53]. The presence of α-Mn_2O_3 can clearly be ruled out, because its characteristic resonance at 542 eV is absent in Fig. 2(b). Instead, the two resonances at 539.4 and 540.8 eV and the one at 548 eV are characteristic for Mn_3O_4, but absent in α-Mn_2O_3. However, the spectra of γ-Mn_2O_3 and Mn_3O_4 are very similar and can hardly be distinguished [54]. This similarity originates from nearly identical geometric struc-

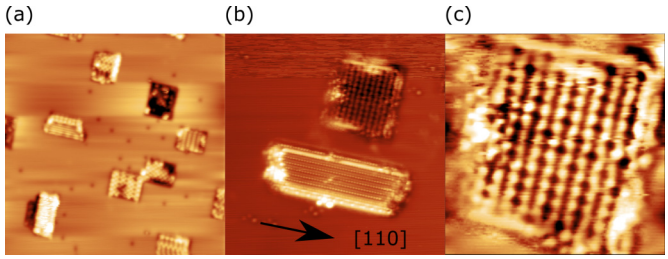

FIG. 3. STM images of an ultrathin Mn_3O_4 film on Ag(001). Mn coverage: 0.3 Mn/Ag. (a) ($50 \times 50\,nm^2$, +1.5 V, 0.1 nA), (b) ($20 \times 20\,nm^2$, −0.2 V, 0.7 nA), (c) detail of the upper island in (b) with increased contrast ($7 \times 7\,nm^2$, −0.2 V, 0.7 nA).

tures with marginal differences in bond lengths and angles. The two oxides differ only in the occupation of octahedral and tetrahedral sites by Mn ions. Therefore γ-Mn_2O_3 can be considered a vacancy structure of Mn_3O_4. In the subsequent discussion we will refer to Mn_3O_4 whereby including γ-Mn_2O_3.

Compared to the NEXAFS spectra of MnO, the absorption onset in the Mn_3O_4 spectra is shifted characteristically to a lower photon energy. This shift has been attributed to the partial occupation of the spin-up $3e_g \uparrow$ states [48,49]. Contrary to MnO, the NEXAFS spectra of the Mn_3O_4 film strongly depend on the angle of light incidence, i.e., there is a pronounced linear dichroism. This sheds some doubt on the current peak assignment to $3e_g$ and $2t_{2g}$ states [48,49], because the dichroism requires lifting the degeneracy of e_g states for octahedral Mn^{3+} ions. However, this discussion is beyond the scope of this publication.

Independent of the details of peak assignment, the pronounced linear dichroism itself supports our epitaxy considerations from above: The tetragonal unit cell [Figs. 1(b) and 1(c)] of the bulk structure of Mn_3O_4 and the small mismatch between the substrate lattice and the two a axes of Mn_3O_4 suggest that the c axis is aligned to the surface normal. The combination of such an alignment and the Jahn-Teller distortion in the direction of the c-axis, in particular the longer distance between octahedral Mn^{3+} and axial O^{2-} ions, imply such a NEXAFS linear dichroism in the energy range close to the O K edge, where empty Mn $3d$ states are involved.

B. Initial stages of island growth

The initial stages of film growth for Mn_3O_4 on Ag(001) have been characterized by STM. An amount of 0.3 Mn/Ag has been deposited at a substrate temperature of 450 K in 2×10^{-6} mbar oxygen within a deposition time of 4 minutes. This equates to a deposition rate of 0.075 Mn/Ag min^{-1}. Without further annealing, separate Mn_3O_4 islands are formed on the Ag substrate (Fig. 3). Taking into account the area ratio of islands and bare Ag, the average island height becomes 0.71 nm, which corresponds to 6 sublayers. Their apparent height is considerable smaller with some island surfaces even below the surrounding Ag(001) surface. As found with NiO and CoO films on Ag(001) [55,56], the islands must be immersed into the Ag surface. This immersion results from the high degree of surface diffusion of Ag, the low surface energy of the Ag surface, and the high energies of island edges.

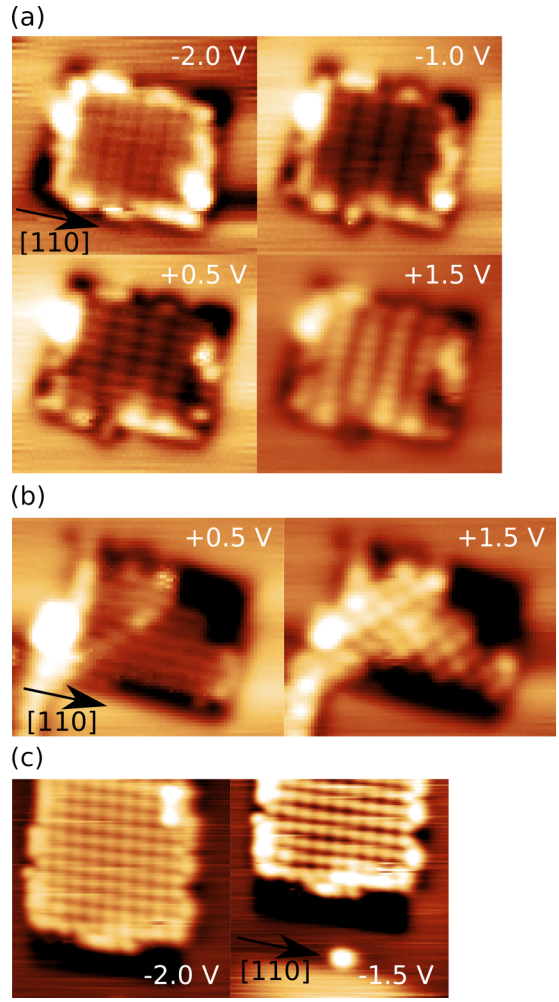

FIG. 4. STM images of three Mn_3O_4 islands for different tunneling voltages. Mn coverage: 0.3 Mn/Ag. (a) $9 \times 8\,nm^2$, 0.1 nA, (b) $10 \times 8\,nm^2$, 0.1 nA, and (c) $7 \times 7\,nm^2$, 0.1 nA.

Most islands have a square shape and exhibit either $p(4 \times 2)$ or $c(4 \times 4)$ reconstructions. Based on atomically resolved STM images of the plain Ag(001) surface (not shown here), the island edges run along ⟨110⟩ directions of the Ag(001) substrate, again similar to NiO and CoO films on Ag(001) [55]. Both reconstructions can be derived from a $p(2 \times 2)$ superstructure by forming alternating long and short distances with bright protrusions and prominent dark depressions most evident in Fig. 3(c).

A second type of islands is rectangularly shaped with a well-resolved striped atomic pattern aligned along ⟨110⟩ directions of the Ag(001) substrate as shown in the bottom part of Fig. 3(b). The island edges parallel to the stripes are long and smooth while those in perpendicular direction are short, tilted by 30°, and rough. The atomic pattern exhibit $p(2 \times 1)$ reconstructions with respect to the Ag substrate. These islands as well as some with increased apparent height without resolved structure appear less frequent than the square ones.

Figure 4 shows STM images of three square islands for different tunneling voltages. For all four voltages [Fig. 4(a)] the first island shows a $p(4 \times 2)$ reconstruction with the $\times 4$ periodicity along [110] and the $\times 2$ periodicity along $[1\bar{1}0]$. At

−2.0 V the protrusions along [110] are not equally spaced, but with long and short separations. This characterizes the transition from $p(2 \times 2)$ to $p(4 \times 2)$. For the other three voltages, the short separation is no longer resolved and the two close protrusions merge to one. At −1.0 and +0.5 V, the elongation along [110] is still obvious, but at +1.5 V it vanishes whereas the contrast is enhanced. This implies that the tunneling at +1.5 V involves different states. A similar change in STM images has also been observed for Fe_3O_4 films [30].

The second type of islands [Fig. 4(b)] presents lines along [110] at +0.5 V, but zig-zag lines at +1.5 V, which correspond to a $c(4 \times 4)$ reconstruction. At +1.5 V the contrast of the island is enhanced in the same way as with the island of Fig. 4(a), irrespective of the difference in surface reconstruction, i.e., $p(4 \times 2)$ versus $c(4 \times 4)$. The common contrast enhancement indicates the presence of the same states in both reconstructions.

The island in Fig. 4(c) resembles the island shown in Fig. 3(c). Interestingly, the strong contrast with dark depressions, which are characteristic for the $p(4 \times 2)$ and $c(4 \times 4)$ reconstructions, is present only at −1.5 V. At this voltage, the image shows alternating separations along $[1\bar{1}0]$ with a phase shift between the right and left part of the island, whereas at −2.0 V the reconstruction resembles a $p(2 \times 2)$ superstructure. Unfortunately, the resolution shown is not always obtained. Therefore the image differences may not originate from different electronic structures of the islands but also from a changed tip state.

In summary, we have found islands with just one of the two surface reconstructions [$p(4 \times 2)$ and $c(4 \times 4)$] as well as islands with a mixture of both. The reported $p(2 \times 5)$ reconstruction [39] has not been observed in our investigations. We attribute this to a complex reconstruction landscape, which spans over deposition rates, oxygen partial pressure, substrate temperature and maybe even treatment history of the substrate. The imaging of these reconstructions via STM is a difficult task, because of the strong dependence on tunneling voltage as well as state of the tunneling tip.

For the interpretation of the STM images, we start with a hard sphere model of the bulk Mn_3O_4(001) unit cell as depicted in Fig. 1(b). The bulk structure of Mn_3O_4(001) is composed of a sequence of two types of sublayers, both with a square unit cell [Fig. 1(d)]. One type consists of a single manganese ion (odd sublayers). The other type contains oxygen and manganese ions with a formal Mn_2O_4 composition [even sublayers in Fig. 1(d)]. For brevity, we will call this sublayer MnO_2 sublayer. These sublayers are stacked alternatingly whereby consecutive sublayers of the same type are laterally displaced by a/2 and rotated by 90°. The stack of eight sublayers (four of each type) form the complete unit cell with an overall height of $c = 944.2$ pm [23].

The interface between film and substrate can have two different terminations. The even MnO_2 sublayer matches the close packed Ag(001) surface much better than the rather open odd sublayer with just a single Mn ion. The arrangement of ions with the even sublayer at the interface is shown in Fig. 1(e). The square unit cell of Mn_3O_4 is arranged along ⟨110⟩ directions of the Ag(001) substrate. This orientation leads to a nearly perfect match of the Mn_3O_4(001) and Ag(001) lattices. So far, we have neither experimental nor theoretical evidence for the registry shift of the two lattices at the interface, i.e., the location of atoms and ions at the interface. In analogy to what was found for CoO on Ag(001) [57], we favor O ions on top of Ag atoms and Mn ions residing in fourfold hollow sites. On top of this mixed MnO_2 interface sublayer, the manganese ions of the second sublayer are in bridge positions above two oxygen ions. Within this scheme, the Mn ions in the mixed MnO_2 sublayer correspond to octahedrally coordinated Mn in the bulk and form a $p(2 \times 1)$ superstructure. The Mn ions of the Mn only sublayer correspond to tetrahedrally coordinated Mn ions in the bulk and form a $p(2 \times 2)$ superstructure. Please note that both reconstructions are given with respect to the unit cell of the Ag(001) substrate surface.

The rectangular island in the bottom part of Fig. 3(b) has characteristic rows of a $p(2 \times 1)$ reconstruction running along the [110] direction of the Ag substrate. The observed arrangement is identical to the $p(2 \times 1)$ reconstruction of an even MnO_2 sublayer. This structure is supported by a theoretical investigation, which predicts that the energy of the MnO_2 termination is significantly lower than the single Mn ion termination [36].

The square island of Fig. 3(c) exhibits protrusions, arranged approximately in a $p(2 \times 2)$ pattern. Again, small lateral shifts create $p(4 \times 2)$ and $c(4 \times 4)$ reconstructions, most obvious when looking at the large dark depressions. We attribute these reconstructions to the presence of subsurface cation vacancies (SCVs) as found on the surface of Fe_3O_4 [30]. Please note, that the $c(2 \times 2)$ reconstruction reported in Ref. [30] refers to Fe_3O_4 and is equivalent to our $c(4 \times 4)$ reconstruction being referred to the Ag(001) substrate.

The concept of surface cation vacancies (SCVs) provides a simple explanation for the reconstructions observed with ultrathin Mn_3O_4 films. Figure 5 presents hard sphere models of the three outermost sublayers of Mn_3O_4 on Ag(001). The three panels on the left, Fig. 5(a), present the model without SCVs. It is build up from three unmodified sublayers as shown in Fig. 1. The bottom panel starts with an MnO_2 sublayer with octahedral Mn ions (blue spheres). In the center panel the second outermost sublayer with tetrahedral Mn ions (turquoise spheres) is added. The top panel shows all three sublayers including a surface termination with an MnO_2 sublayer. The Mn and O ions of the top sublayer form the $p(2 \times 1)$ reconstruction as indicated by the black rectangle in the top panel, whereby neglecting ions in the second and third outermost sublayers. Presumably, this $p(2 \times 1)$ reconstruction is present in the lower island of Fig. 3(b).

The three panels on the right, Fig. 5(b), present the model with SCVs. We start with the third outermost sublayer in the bottom panel of Fig. 5(b). The removal of Mn ions from the sublayer along the ×1 periodicity can be done either with [upper part of the bottom panel in Fig. 5(b)] or without lateral offset between horizontal rows of Mn ions and vacancies (lower part of the bottom right panel). For two removed octahedral Mn ions (blue spheres) one interstitial tetrahedral Mn ion (turquoise spheres) is added in the second sublayer directly above the vacancy. These interstitial Mn ions implicate a reconstruction of the MnO_2 terminated surface. With lateral offset, the alternating rows form a $c(4 \times 4)$ reconstruction as can be seen in the center panel of Fig. 5(b) (upper part).

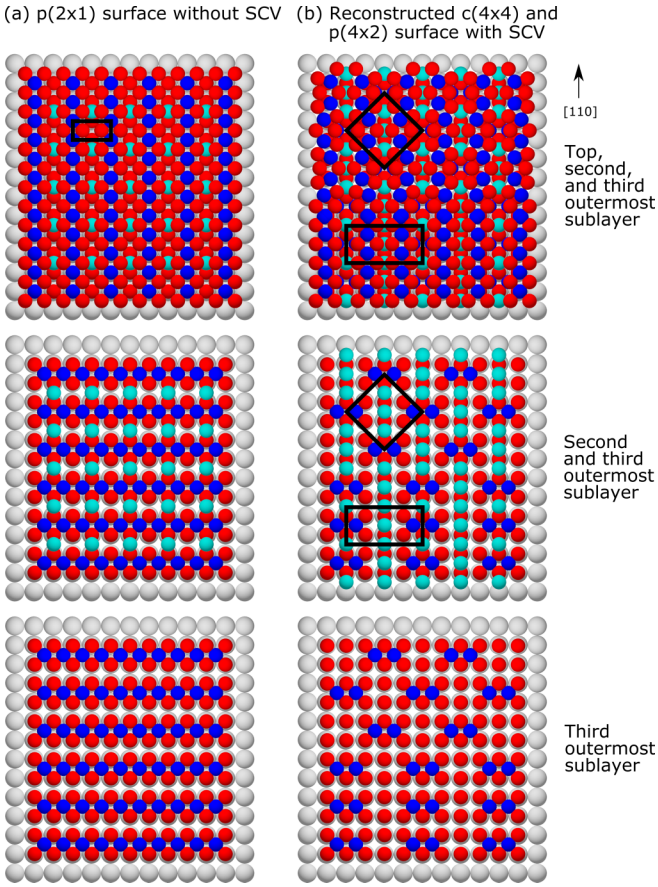

FIG. 5. Arrangements for the three outermost sublayers of Mn_3O_4 on Ag(001) for (a) the unreconstructed surface and (b) the reconstructed surface with subsurface cation vacancies. Hard sphere model with Ag (grey), O (red), octahedrally coordinated Mn (blue), and tetrahedrally coordinated Mn (turquoise). The unit cells of the surface reconstructions are marked in black.

Without offset, the rows of the SCVs are nonalternating and lead to a $p(4 \times 2)$ reconstruction, as indicated by the black rectangle in the lower part of the center panel.

In the top panel of Fig. 5(b), the top MnO_2 sublayer is added. The SCVs in the third outermost sublayer and the additional Mn ions in the second outermost sublayer lead to small lateral shifts of the Mn and O ions in the top layer. The structure shown is only a tentative model for illustration. The $c(4 \times 4)$ and $p(4 \times 2)$ reconstructions resemble the structures imaged in the lower part of Fig. 3(c) and the island in Fig. 6(c). The $p(4 \times 2)$ reconstruction becomes particularly obvious by the alternating intensities of the dark sites between the bright protrusions.

The presence of SCVs is supported by the fact that their creation mechanism, namely the removal of two octahedral Mn ions, the addition of one tetrahedral Mn ion, and the diffusion of one Mn ion to the surface, represents the structural transition between the bulk phases of MnO and Mn_3O_4, and probably also between Mn_3O_4 and γ-Mn_2O_3. Thus we interpret the appearance of SCVs as the beginning of this transition from Mn_3O_4 to γ-Mn_2O_3 in the close proximity of the surface. Contrary to Fe_3O_4, the Jahn-Teller effect in Mn_3O_4 makes the equatorial and axial bond lengths of the

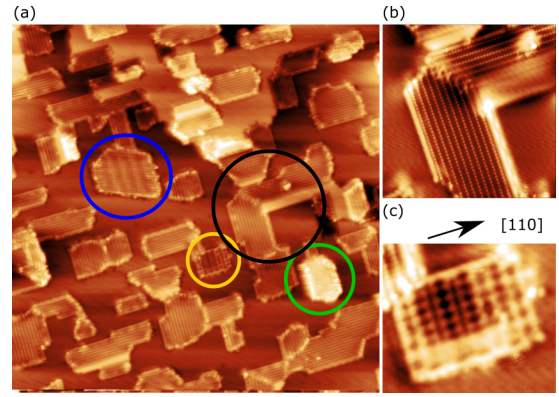

FIG. 6. STM images of an ultrathin Mn_3O_4 film on Ag(001). Mn coverage: 1 Mn/Ag. (a) ($60 \times 60\,nm^2$, +1.3 V, 0.2 nA), (b) close up of the island marked in (a) with a black circle ($15 \times 15\,nm^2$, +0.9 V, 0.2 nA), (c) close up of the island marked in (a) with a yellow circle ($7 \times 6\,nm^2$, +1.0 V, 0.2 nA).

octahedral site quite different. The short equatorial bond lengths (193.0 pm) imply strong bonds; the long axial bond lengths (228.2 pm) weak bonds [23]. The weak axial bonds as well as the fact, that the oxygen lattice is not as close packed as in Fe_3O_4, may facilitate the transitions from MnO to Mn_3O_4 and γ-Mn_2O_3, because Mn ions can diffuse more readily within the lattice, in particular between octahedral and tetrahedral sites.

As mentioned in the introduction, the structural differences between Mn_3O_4 and γ-Mn_2O_3 do not yield major differences neither in NEXAFS spectra nor in diffraction patterns. On surfaces, however, SCVs are accompanied by reconstructions, which offers a better chance to monitor them by STM investigations.

C. Islands at a coverage of 1 Mn ion per Ag atom

In the following, the film growth for increased amounts of manganese will be discussed. The amount of 1 Mn/Ag has been deposited at room temperature in 2×10^{-6} mbar oxygen within a deposition time of 50 minutes. This equates to a low deposition rate of 0.02 Mn/Ag min^{-1}. Assuming bulk structure of Mn_3O_4 results in 6.3 pm/min. After deposition, the sample was annealed to 640 K in UHV.

Assuming an MnO_2 sublayer at the interface and layer by layer growth, 1 Mn/Ag corresponds to 21 2 sublayers, the MnO_2 sublayer at the interface, one Mn sublayer and half of an MnO_2 sublayer. However, the STM image in Fig. 6 shows four different kinds of Mn_3O_4 islands, which do not cover the complete substrate surface. The bare Ag surface is still present between the islands. Taking into account the area ratio between islands and bare Ag, the average island height corresponds to 6 sublayers. Thus the island height is comparable to the one for the islands in Fig. 3, although the total amount of manganese on the substrate is more than tripled. Over 80% of the islands in Fig. 6(a) have a $p(2 \times 1)$ reconstruction as is better seen for the island marked with a black circle in Fig. 6(a) and in the enlarged image in Fig. 6(b).

The other three island types are $p(2 \times 1)$ islands rotated by 20° [blue circle in Fig. 6(a)], islands with an increased

TABLE I. Summary of preparation conditions and resulting superstructures. All preparations: O_2 partial pressure during deposition: 2×10^{-6} mbar; annealing: UHV conditions. Surface cation vacancies (SCVs) have been derived from and stand for the presence of $p(4 \times 2)$ and $c(4 \times 4)$ superstructures. In the calculation of the deposited amount of Mn ions given in sublayers, an interface layer of MnO_2 is assumed. *Incremental deposition onto previous preparation.

Deposited Amount of Mn Ions		Deposition Rate	Deposition Temperature	Annealing Temperature	Free Ag Surface	Island Height	Surface Reconstruction
$\left(\frac{\text{Mn}}{\text{Ag}}\right)$	(sublayers)	$\left(\frac{\text{Mn}}{\text{Ag min}}\right)$	(K)	(K)	(%)	(sublayers)	
0.3	0.6	0.075	450	–	85	5	SCVs (few 2×1)
1	2.5	0.02	295	640	50	5	2×1 (few SCVs)
2	5	0.08	295	640	30	7	2×1
4 (2+2)*	10.5	0.08	295	640	0	10.5	2×1
5 (2+2+1)*	13	0.08	295	640	0	13	$2 \times 1 +$ SCVs
10 (2+2+1+5)*	26.5	0.08	295	740	0	26.5	$2 \times 1 +$ SCVs

apparent height without resolved surface structure [green circle in Fig. 6(a)] and nearly square islands aligned along ⟨110⟩ directions [yellow circle in Fig. 6(a) and enlarged image in Fig. 6(c)]. On first glance, these islands exhibit a $p(2 \times 2)$ reconstruction. However, along the [110] direction there are alternating long and short distances. This results in a $p(4 \times 2)$ reconstruction with prominent dark depressions. The triangular shape of the bright protrusions indicates that the local coordination of Mn is different from the fourfold one in bulk. Assuming a stoichiometry of MnO_2 for the surface sublayer, each protrusion corresponds to 2 Mn ions, which explains the elongated shape. The same observation has also been reported for the SCV-stabilized surface of Fe_3O_4 [30].

These results show that different kinds of islands coexist over a wide range of preparation conditions whereby either rectangular $p(2 \times 1)$ islands [Fig. 6(a)] or square $p(4 \times 2)$ and $c(4 \times 4)$ islands [Fig. 3(a)] are favored. Possible reasons for the differences are annealing temperature, deposition rate, and amount of material. In the low coverage regime a slow deposition with a subsequent UHV annealing to 640 K favors the $p(2 \times 1)$ reconstruction without SCVs. For increased deposition rates and lower annealing temperatures, the three outermost sublayers are stabilized by subsurface cation vacancies as reported for Fe_3O_4 [30]. This is indicated by the presence of $p(4 \times 2)$ and $c(4 \times 4)$ reconstructions. It should be pointed out that the termination sublayer for all observed islands is assumed as MnO_2. With an MnO_2 sublayer at the interface, the minimal island height observed corresponds to 5 or 7 sublayers. This height is sufficient for the formation of SCVs with a reconstruction of the three outermost sublayers as shown in Fig. 5(b).

D. Coverages of 2 and 4 Mn ions per Ag atom

Figure 7 shows STM images, a LEED pattern, and sublayer schemes for depositions of 2 and 4 Mn/Ag with a rate of 0.08 Mn/Ag min^{-1} at room temperature in 2×10^{-6} mbar oxygen. After deposition, the films were annealed to 640 K to increase film quality. The 4 Mn/Ag film has been formed by incrementally depositing additional 2 Mn/Ag onto the film with 2 Mn/Ag under the same conditions and followed by UHV annealing.

Assuming an MnO_2 sublayer at the interface and layer by layer growth a coverage of 2 Mn/Ag corresponds to five sublayers. The STM image of this film in Fig. 7(a) shows Mn_3O_4 islands with $p(2 \times 1)$ stripes surrounded by flat Ag areas. The Mn_3O_4 islands cover only 70% of the surface. Therefore the local island height corresponds to seven sublayers, i.e., close to one unit cell. Exactly as at low coverage, the $p(2 \times 1)$ islands show rectangular shapes with long edges running along ⟨110⟩ directions of the Ag(001) substrate (compare to Fig. 6). The same kind of islands is also observed rotated by 90°, in line with the fourfold symmetry of the Ag(001) substrate. Where such islands meet, they form domain boundaries along ⟨100⟩ directions.

The $p(4 \times 2)$ and $c(4 \times 4)$ reconstructions, which are typical for SCV-reconstructed islands, have not been observed. Table I summarizes preparations and surface reconstructions. The lower the deposition rate, the more Mn^{3+} ions and SCVs are expected. However, the results show that a deposition rate of 0.08 Mn/Ag min^{-1} is low enough for the creation of SCVs and γ-Mn_2O_3. Increasing the oxygen partial pressure is

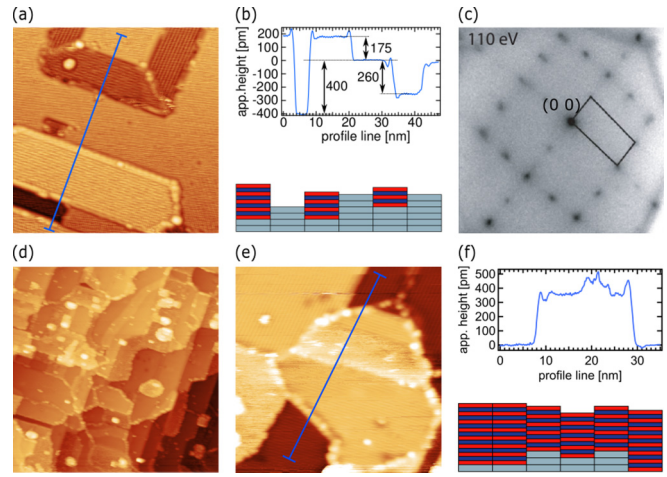

FIG. 7. Ultrathin Mn_3O_4 films on Ag(001). (a) Mn coverage: 2 Mn/Ag. STM image for $37 \times 37\,\text{nm}^2$, +2.0 V, 0.8 nA, (b) height profile along the blue line from the STM image (a) and sublayer scheme of the film, and (c) corresponding LEED pattern with a $p(2 \times 1)$ unit cell. (d) Mn coverage: 4 Mn/Ag. STM image for $120 \times 120\,\text{nm}^2$, +1.3 V, 0.8 nA, (e) detailed STM image ($35 \times 35\,\text{nm}^2$, +1.5 V, 0.5 nA), and (f) height profile along the blue line from the STM image (e) and corresponding scheme with an average of 12 sublayers on a Ag substrate.

expected to favor Mn^{3+} ions and SCVs, but we kept it constant and did not further investigate this. The effect of deposition rate and annealing temperatures on the creation of SCVs could be in either direction. On one hand, higher temperatures favor the desorption of oxygen and the formation of Mn^{2+} ions. On the other hand, higher temperatures also favor the diffusion of Mn ions to the surface and the creation of SCVs as long as sufficient oxygen is available for the balance of Mn^{3+} ions. The build-up of the islands with large areas of free Ag surface indicates that the mobility of Mn ions is large even at 450 K. SCVs are mainly present at very low coverages and to some extend at high coverages. This indicates that the interface stabilizes SCVs. However, the data taken so far can only serve as a first step for a detailed understanding.

Different step heights can be found in the line profile of Fig. 7(b). A height of 400 pm corresponds to the Ag(001) unit cell (a_{Ag} = 409 pm). The values of 260 and 175 pm are much smaller than the expected island height of about one Mn_3O_4 unit cell (944.2 pm [23]). This indicates that the Mn_3O_4 islands are embedded into the Ag substrate as illustrated schematically in Fig. 7(b). A direct assignment of island heights is not straight forward, because local island heights and/or depths of embedding influence the tunneling current, i.e., image brightness. For a detailed, quantitative analysis, the electronic structure of the Mn_3O_4 islands needs to be known and taken into account, as has been shown for CoO on Ag(001) [58].

The LEED pattern of the film with a coverage of 2 Mn/Ag shown in Fig. 7(c) gives information about the integral structure of the sample. One can recognize a $p(2 \times 1)$ reconstruction with two domains rotated by 90°. In agreement to the STM images, no additional spots have been found at any electron energy, specifically there are no $(\frac{1}{2}\ \frac{1}{2})$ spots of a $p(2 \times 2)$ reconstruction.

The LEED pattern of the film with a coverage of 4 Mn/Ag is identical to the one with 2 Mn/Ag. Also, the STM images for the 4 Mn/Ag film are similar with patches of 90° rotated $p(2 \times 1)$ domains [Figs. 7(d) and 7(e)]. Because of the increased film thickness the Ag(001) substrate is now completely covered with Mn_3O_4 and bare substrate areas are not observed anymore. The step heights in the line profile in Fig. 7(f) from the STM image in Fig. 7(e) are much smaller than the average island height of 10 sublayers, i.e., 1.2 nm. Presumably, they result from a combination of substrate steps and islands heights as illustrated schematically in Fig. 7(f). The step height of 370 pm between Mn_3O_4 terraces is actually close to a double step height of the Ag(001) substrate (409 pm). In addition, patches without atomic resolution but increased heights are present. Presumably, the increased island heights of these patches are accompanied by changes in their electronic structure or different surface reconstructions.

E. Coverages of 5 and 10 Mn ions per Ag atom

One additional Mn ion per Ag atom has been deposited onto the 4 Mn/Ag film at room temperature under the same preparation conditions as before. After subsequent annealing to 640 K one can distinguish four different structures in the STM image of Fig. 8(a) that coexist in close proximity. The

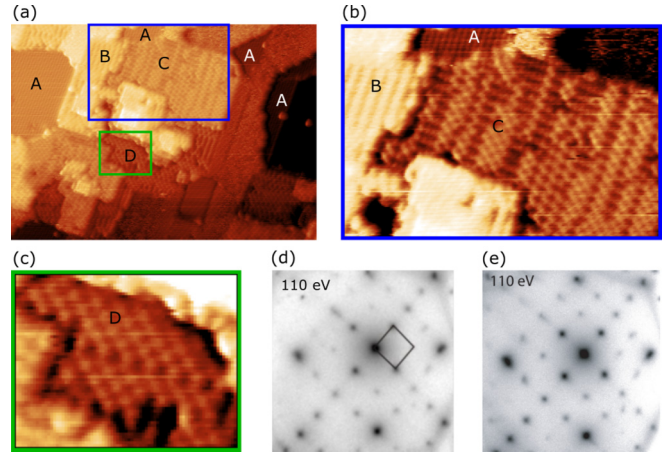

FIG. 8. (a) STM image of an Mn_3O_4 film on Ag(001) (coverage: 5 Mn/Ag) (58 × 47 nm^2, +2.0 V, 0.3 nA, Δz = 2 nm). (b) and (c) STM details of (a), FFT filtered (blue 25 × 19 nm^2, green 9 × 8 nm^2). Capital letters mark different reconstructions at the surface as detailed in text section E. SPA-LEED patterns at 110 eV for (d) a film with 5 Mn/Ag after annealing to 640 K and (e) a film with 10 Mn/Ag after annealing to 740 K.

flat regions A show stripes with ×2 periodicity. We assign them to the $p(2 \times 1)$ reconstruction with the ×1 periodicity unresolved. Region B has similar stripes, but with ×4 periodicity. Since a $p(4 \times 2)$ reconstruction could be resolved in region C, we assign these stripes to a $p(4 \times 1)$ reconstruction. Region C is a complex mix of $p(4 \times 2)$ and $c(4 \times 4)$ elements. The related region D shows two domains with $c(4 \times 4)$. As above, we propose that these reconstructions originate from SCVs. Small displacements of the ×2 lines in region D suggest that there also exists an SCV with a lateral displacement by just one sublattice unit [instead of two for the $c(4 \times 4)$]. As for the film with a coverage of 4 Mn/Ag, there are still patches without atomic resolution next to ordered surface reconstructions.

Surprisingly, the corresponding LEED pattern [Fig. 8(d)] shows spots of a $p(2 \times 2)$ reconstruction only (marked black unit cell), contrary to the $p(2 \times 1)$, $p(4 \times 2)$, and $c(4 \times 4)$ reconstructions found using STM. In particular, no $\frac{1}{4}$ order spots were found in agreement with Kundu *et al.* [39]. There are a number of explanations for such puzzling findings. First, the large and intense halos around the peaks and the streaks along ⟨110⟩ directions indicate considerable disorder. Second, the larger escape depth of electrons at 110 eV (compared with the 40 eV used in Ref. [39]) increases the diffraction contribution from $p(2 \times 1)$ subsurface layers. Third, LEED I-V interferential effects from the atomic structure may extinguish a family of diffraction spots. Although $p(4 \times 2)$ and $c(4 \times 4)$ symmetry phases cannot exhibit glide planes, a similar extinction of spots originates from lateral shifts between domains by half a unit cell in case the domains are considerably smaller than the transfer length of the LEED optics. Finally, reconstructions might be present outside the region of the STM image. However, without further evidence, all remain quite speculative. Taking the $p(2 \times 1)$ reconstruction of the films with 2 and 4 Mn/Ag (Fig. 7) as a starting point, we assign the apparent $p(2 \times 2)$ reconstruction to a superpo-

sition of $p(2 \times 1)$ and $c(2 \times 2)$ reconstructions. Interestingly, a $c(2 \times 2)$ reconstruction is not compatible with tetrahedral Mn ions in a simple way, i.e., its actual presence indicates the existence of tetrahedral cation vacancies.

Finally, another 5 Mn/Ag have been deposited on the film. The increased thickness of the film allows annealing up to 740 K without rupture of the film. The LEED pattern in Fig. 8(e) shows basically the same $p(2 \times 2)$ superstructure of Mn_3O_4 as Fig. 8(d). Probably, it stems from the same surface reconstructions. A more detailed comparison shows increased LEED spot intensities indicating a higher area fraction of well ordered Mn_3O_4 islands as a result of the higher annealing temperature. Furthermore, the increase of the $(\frac{1}{2}\ \frac{1}{2})$ spots intensities appears slightly stronger than that of the $(1\ \frac{1}{2})$ spots. This points to a higher fraction of the $c(2 \times 2)$ reconstruction. Unfortunately, no well-resolved STM images could be obtained at this film thickness to approve or disapprove the presence of these reconstructions.

Based on these observations, the growth behavior of Mn_3O_4 for a fixed annealing temperature of 640 K can be described as follows: Up to a coverage of 4 Mn/Ag the surface reconstructs with $p(2 \times 1)$ islands indicating an MnO_2 termination and no presence of SCVs. At a coverage of 5 Mn/Ag a mixture of different surface reconstructions gives evidence of the coexistence of domains with and without SCVs. At 10 Mn/Ag, the LEED pattern suggests similar reconstructions. However, no STM images could be obtained to confirm this. A similar growth mode has also been observed for the system Fe_3O_4 on Fe(100) [59]. For a thickness below one unit cell only a $p(2 \times 1)$ can be observed in the LEED pattern, while for thicker films SCVs stabilize the reconstructed surface.

The driving force for the structural transition in the MnO_2 top sublayer is supposedly a decrease in surface energy. Together with expansion and perfection of the SCV reconstruction, the amount of polar-edged $p(2 \times 1)$ islands decreases. Consequently, the densities of rotated $p(2 \times 1)$ domains and domain walls are expected to decrease. This leads to a lower interface energy for the $p(4 \times 2)$ and $c(4 \times 4)$ reconstructions.

IV. CONCLUSIONS

The growth of ultrathin Mn_3O_4(001) films on Ag(001) has been investigated from initial stages up to coverages of 10 Mn/Ag by a combination of near-edge x-ray absorption fine structure spectroscopy, scanning tunneling microscopy, and low-energy electron diffraction. By means of NEXAFS the linear dichroism at the oxygen K absorption edge was examined to clearly distinguish MnO from Mn_3O_4 and to derive the orientation of the Mn_3O_4 film. Different reconstructions of the MnO_2-terminated surface of Mn_3O_4 have been determined by STM depending on annealing temperature and coverage. In particular, Mn_3O_4 islands with a $p(2 \times 1)$ reconstruction and subsurface cation vacancies inducing the local formation of $p(4 \times 2)$ and $c(4 \times 4)$ reconstructions have been identified. The $p(2 \times 1)$ islands are favored for a coverage up to 4 Mn/Ag and an annealing temperature of 640 K. The reconstructed surface with subsurface cation vacancies develops for a coverage of 5 Mn/Ag and annealing to 640 K or at the initial stages of film formation with a reduced annealing temperature of 450 K. All islands exhibit edges aligned along $\langle 110 \rangle$ directions and grow embedded into the Ag substrate.

This is the second description of subsurface cation vacancies beyond the system Fe_3O_4 and delivers further insight into the formation of such vacancies. Depending on the offset between vacancy sites, different surface reconstructions as $p(4 \times 2)$ or $c(4 \times 4)$ develop. With the creation of octahedral vacancies and additional Mn ions on tetrahedral interstitial sites, the formation of subsurface cation vacancies corresponds to the transition of bulk Mn_3O_4 to γ-Mn_2O_3.

Note added. Recently, the same line of arguments from the NEXAFS linear dichroism to the orientation of Mn_3O_4 films has been given in Ref. [60].

ACKNOWLEDGMENTS

Financial support from the Deutsche Forschungsgemeinschaft (DFG) through the collaborative research centers SFB 762 “Functionality of Oxide Interfaces” (projects A3 and A7) and SFB/TRR 227 “Ultrafast Spin Dynamics” (Project-ID 328545488 - TRR 227, project A06) is gratefully acknowledged. The authors highly acknowledge scientific discussions as well as the mutual technical support within the SFB and thank B. Zada and W. Mahler from the beamline UE56-2 PGM-2 at the synchrotron BESSY II, Berlin for their assistance. Particular thanks goes to R. Kulla for his technical assistance during experiments.

K.G. and M.T. contributed equally to this work.

[1] M. Bäumer, D. Cappus, H. Kuhlenbeck, H.-J. Freund, G. Wilhelmi, A. Brodde, and H. Neddermeyer, Surf. Sci. **253**, 116 (1991).

[2] G. A. Rizzi, M. Petukhov, M. Sambi, R. Zanoni, L. Perriello, and G. Granozzi, Surf. Sci. **482-485**, 1474 (2001).

[3] C. Hagendorf, S. Sachert, B. Bochmann, K. Kostov, and W. Widdra, Phys. Rev. B **77**, 075406 (2008).

[4] S. Sachert, S. Polzin, K. Kostov, and W. Widdra, Phys. Rev. B **81**, 195424 (2010).

[5] Y. Martynova, M. Soldemo, J. Weissenrieder, S. Sachert, S. Polzin, W. Widdra, S. Shaikhutdinov, and H. J. Freund, Catal. Lett. **143**, 1108 (2013).

[6] F. Allegretti, C. Franchini, V. Bayer, M. Leitner, G. Parteder, B. Xu, A. Fleming, M. G. Ramsey, R. Podloucky, S. Surnev, and F. P. Netzer, Phys. Rev. B **75**, 224120 (2007).

[7] C. Franchini, R. Podloucky, F. Allegretti, F. Li, G. Parteder, S. Surnev, and F. P. Netzer, Phys. Rev. B **79**, 035420 (2009).

[8] C. Franchini, J. Zabloudil, R. Podloucky, F. Allegretti, F. Li, S. Surnev, and F. P. Netzer, J. Chem. Phys. **130**, 124707 (2009).

[9] F. Li, G. Parteder, F. Allegretti, C. Franchini, R. Podloucky, S. Surnev, and F. P. Netzer, J. Phys.: Condens. Matter **21**, 134008 (2009).

[10] H. Nishimura, T. Tashiro, T. Fujitani, and J. Nakamura, J. Vac. Sci. Technol. A **18**, 1460 (2000).

[11] L. Zhang, Z. Tang, S. Wang, D. Ding, M. Chen, and H. Wan, Surf. Sci. **606**, 1507 (2012).

[12] C. Möller, J. Barreto, F. Stavale, and N. Nilius, J. Phys. Chem. C **123**, 7665 (2019).

[13] F. Müller, R. de Masi, D. Reinicke, P. Steiner, S. Hüfner, and K. Stöwe, Surf. Sci. **520**, 158 (2002).

[14] M. Nagel, I. Biswas, H. Peisert, and T. Chassé, Surf. Sci. **601**, 4484 (2007).

[15] M. Nagel, I. Biswas, P. Nagel, E. Pellegrin, S. Schuppler, H. Peisert, and T. Chassé, Phys. Rev. B **75**, 195426 (2007).

[16] A. Chassé, C. Langheinrich, F. Müller, and S. Hüfner, Surf. Sci. **602**, 597 (2008).

[17] E. A. Soares, R. Paniago, V. E. de Carvalho, E. L. Lopes, G. J. P. Abreu, and H.-D. Pfannes, Phys. Rev. B **73**, 035419 (2006).

[18] A. K. Kundu and K. S. R. Menon, J. Cryst. Growth **446**, 85 (2016).

[19] A. K. Kundu, S. Barman, and K. S. R. Menon, Phys. Rev. B **96**, 195116 (2017).

[20] A. Chassé, C. Langheinrich, M. Nagel, and T. Chassé, Surf. Sci. **605**, 272 (2011).

[21] The deposition rates for MnO and Mn_3O_4 films are cited as given in the literature. However, comparing rates in Å/min requires particular care, because the number of Mn ions per angstroms in Mn_3O_4 films is lower than the one in MnO films by a factor of 0.7. The influence of vacancies and strains on the structures pose additional, but usually neglected difficulties. In order to avoid these problems, we use Mn ions per substrate Ag atom wherever possible.

[22] B. Morosin, Phys. Rev. B **1**, 236 (1970).

[23] D. Jarosch, Mineral. Petrol. **37**, 15 (1987).

[24] S. Pal and S. Lal, Phys. Rev. B **96**, 075139 (2017).

[25] J. B. Goodenough and A. L. Loeb, Phys. Rev. **98**, 391 (1955).

[26] K. P. Sinha and A. P. B. Sinha, J. Phys. Chem. **61**, 758 (1957).

[27] J. Kaczmarek and E. Wolska, J. Solid State Chem. **103**, 387 (1993).

[28] C. Greaves, J. Solid State Chem. **49**, 325 (1983).

[29] M. Boudeulle, H. Batis-Landoulsi, C. LeClercq, and P. Vergnon, J. Solid State Chem. **48**, 21 (1983).

[30] R. Bliem, E. McDermott, P. Ferstl, M. Setvin, O. Gamba, J. Pavelec, M. A. Schneider, M. Schmid, U. Diebold, P. Blaha, L. Hammer, and G. S. Parkinson, Science **346**, 1215 (2014).

[31] S. Huang, Y. Wang, Z. Wang, K. Zhao, X. Shi, X. Lai, and L. Zhang, Solid State Commun. **212**, 25 (2015).

[32] G. Wang, S. Wu, W. Zhou, Y. Wang, and S. Li, Mater. Lett. **195**, 86 (2017).

[33] O. Y. Gorbenko, I. E. Graboy, V. A. Amelichev, A. A. Bosak, A. R. Kaul, B. Güttler, V. L. Svetchnikov, and H. W. Zandbergen, Solid State Commun. **124**, 15 (2002).

[34] J. Y. Liu, X. Cheng, V. Nagarajan, and H. L. Xin, MRS Commun. **5**, 277 (2015).

[35] L. Bigiani, C. Maccato, A. Gasparotto, C. Sada, and D. Barreca, Mater. Chem. Phys. **223**, 591 (2019).

[36] V. Bayer, R. Podloucky, C. Franchini, F. Allegretti, B. Xu, G. Parteder, M. G. Ramsey, S. Surnev, and F. P. Netzer, Phys. Rev. B **76**, 165428 (2007).

[37] L. Bigiani, D. Barreca, A. Gasparotto, and C. Maccato, Surf. Sci. Spectra **25**, 014003 (2018).

[38] L. Bigiani, M. Hassan, D. Peddis, C. Maccato, G. Varvaro, C. Sada, E. Bontempi, S. Martí-Sánchez, J. Arbiol, and D. Barreca, ACS Appl. Nano Mater. **2**, 1704 (2019).

[39] A. K. Kundu, S. Barman, and K. S. R. Menon, Surf. Sci. **664**, 207 (2017).

[40] K. Gillmeister, M. Huth, R. Shantyr, M. Trautmann, K. Meinel, A. Chassé, K.-M. Schindler, H. Neddermeyer, and W. F. Widdra, arXiv:1506.07294.

[41] K. Takayanagi, K. Yagi, and G. Honjo, Thin Solid Films **48**, 137 (1978).

[42] M. Pivetta, F. Patthey, M. Stengel, A. Baldereschi, and W.-D. Schneider, Phys. Rev. B **72**, 115404 (2005).

[43] K. Marre and H. Neddermeyer, Surf. Sci. **287–288**, 995 (1993).

[44] C. Ammer, K. Meinel, H. Wolter, A. Beckmann, and H. Neddermeyer, Surf. Sci. **375**, 302 (1997).

[45] R. Hammer, A. Sander, S. Förster, M. Kiel, K. Meinel, and W. Widdra, Phys. Rev. B **90**, 035446 (2014).

[46] K. J. S. Sawhney, F. Senf, M. Scheer, F. Schäfers, J. Bahrdt, A. Gaupp, and W. Gudat, Nucl. Instrum. Methods Phys. Res., Sect. A **390**, 395 (1997).

[47] M. Risch, K. A. Stoerzinger, B. Han, T. Z. Regier, D. Peak, S. Y. Sayed, C. Wei, Z. Xu, and Y. Shao-Horn, J. Phys. Chem. C **121**, 17682 (2017).

[48] H. Kurata and C. Colliex, Phys. Rev. B **48**, 2102 (1993).

[49] D. M. Sherman, Am. Mineral. **69**, 788 (1984).

[50] L. Laffont and P. Gibot, Mater. Charact. **61**, 1268 (2010).

[51] P.-T. Chen, C.-M. Tseng, T.-Y. Yung, M.-W. Chu, C.-H. Chen, and M. Hayashi, Ultramicroscopy **140**, 51 (2014).

[52] B. Gilbert, B. H. Frazer, A. Belz, P. G. Conrad, K. H. Nealson, D. Haskel, J. C. Lang, G. Srajer, and G. De Stasio, J. Phys. Chem. A **107**, 2839 (2003).

[53] F. M. F. de Groot, M. Grioni, J. C. Fuggle, J. Ghijsen, G. A. Sawatzky, and H. Petersen, Phys. Rev. B **40**, 5715 (1989).

[54] S. H. Kim, B. J. Choi, G. H. Lee, S. J. Oh, B. Kim, H. C. Choi, J. Park, and Y. Chang, J. Kor. Phys. Soc. **46**, 941 (2005).

[55] I. Sebastian, T. Bertrams, K. Meinel, and H. Neddermeyer, Faraday Discuss. **114**, 129 (1999).

[56] C. Hagendorf, R. Shantyr, K. Meinel, K.-M. Schindler, and H. Neddermeyer, Surf. Sci. **532–535**, 346 (2003).

[57] K.-M. Schindler, J. Wang, A. Chassé, H. Neddermeyer, and W. Widdra, Surf. Sci. **603**, 2658 (2009).

[58] R. Shantyr, C. Hagendorf, and H. Neddermeyer, Thin Solid Films **464-465**, 65 (2004).

[59] M. Soldemo, M. Vandichel, H. Grönbeck, and J. Weissenrieder, J. Phys. Chem. C **123**, 16317 (2019).

[60] E. Annese, A. Ali, J. Barreto, G. Felix, and F. Stavale, Appl. Surf. Sci. **578**, 151944 (2022).